RESEARCH ARTICLE

Lithium-Ion Batteries

Energy & Environmental Materials WILEY

One-Pot Spray Pyrolysis Fabrication of Multi-Phase Lithium Manganese Oxide Microsphere Cathodes for Enhanced Lithium-Ion Battery Performance

Jae Hyeon Choi, Yeon Oh Lee, Kyoung Sun Kim, Yun Chan Kang, Jung Sang Cho, Hyungsub Kim, Sang Mun Jeong, and Gi Dae Park**

Spinel-type lithium manganese oxide (LMO) cathodes offer low cost, environmental benignity, and strong thermal safety, making them attractive for fast-charge lithium-ion batteries. Their widespread adoption, however, has been hindered by structural degradation associated with the Jahn–Teller distortion of Mn^{3+}. Here, we report for the first time a rapid, single-step spray pyrolysis route that produces multi-phase microspheres comprising Sr-doped $LiMn_2O_4$ spinel, a minor $Sr_2Mn_2O_5$ phase, and a C2/m layered Li_2MnO_3-like structure, all crystallized directly from a single precursor solution without post-treatment. This continuous aerosol process enables uniform Sr incorporation, precise morphological control, and manufacturing scalability. The synergistic coexistence of these phases provides multiple benefits: Sr doping lowers the Mn^{3+} fraction, suppresses lattice distortion, and stabilizes the spinel framework; the $Sr_2Mn_2O_5$ phase refines particle morphology and mitigates mechanical stress during cycling; and the layered Li_2MnO_3-like domains enhance structural stability, diversify Li^+ diffusion pathways, and suppress Mn dissolution and electrolyte side reactions. As a result, the composite cathode delivers improved electrochemical performance, retaining 81.72 mA h g^{-1} after 400 cycles at 1 C and 76.78 mA h g^{-1} at 5 C, demonstrating that rapid, single-step spray pyrolysis is an effective and scalable strategy for robust, high-voltage spinel cathodes.

1. Introduction

Spinel-structured lithium manganese oxide ($LiMn_2O_4$, LMO) is an attractive lithium-ion battery cathode owing to its cost effectiveness, environmental benignity, and three-dimensional Li^+ diffusion pathways that enable high-rate operation within a structurally simple framework.[1–3] However, commercialization remains limited by rapid capacity fading and structural degradation under high-voltage or elevated-temperature cycling.[4,5] These failures originate from the Jahn–Teller distortion of Mn^{3+}, which induces anisotropic lattice strain, and from manganese dissolution that depletes active material and thickens interphases.[6,7] In typical electrolytes, HF generated from $LiPF_6$ decomposition exacerbates Mn^{3+} disproportionation and solubilization, accelerating impedance growth.[8–10] The combined effects trigger mechanical instability, micro-crack initiation and propagation within secondary particles, and loss of electrical percolation across the electrode matrix.

To address these issues, numerous doping strategies, including Ni, Cu, and Sr, have been reported to stabilize the lattice and suppress degradation.[11–15] Yet, most reported approaches involve complex multi-step solid-state reactions, sol–gel or co-precipitation routes followed by prolonged high-temperature annealing, or iterative post-treatments.[16–19] Such process trains compromise scalability, increase energy and time costs, and often yield inhomogeneous dopant distributions or radial concentration gradients. Additionally, excessive substitution by electrochemically inactive species

J. H. Choi, Y. O. Lee, Prof. G. D. Park
Department of Urban, Energy, and Environmental Engineering, Chungbuk National University, Chungdae-ro 1, Seowon-gu, Cheongju 28644, Republic of Korea
E-mail: gdpark@chungbuk.ac.kr
K. S. Kim, Dr. H. Kim, Prof. G. D. Park
Neutron Science Division, Korea Atomic Energy Research Institute (KAERI), Daejeon 34057, Republic of Korea
Prof. Y. C. Kang
Department of Materials Science and Engineering, Korea University, Anam-Dong, Seongbuk-Gu, Seoul 136-713, Republic of Korea
Prof. J. S. Cho
Department of Engineering Chemistry, Chungbuk National University, Chungdae-ro 1, Seowon-gu, Cheongju 28644, Republic of Korea
Prof. J. S. Cho, Dr. H. Kim, Prof. S. M. Jeong, Prof. G. D. Park
Advanced Energy Research Institute, Chungbuk National University, Chungdae-ro 1, Seowon-gu, Cheongju, Chungbuk 28644, Republic of Korea
E-mail: smjeong@chungbuk.ac.kr
Prof. S. M. Jeong
Department of Chemical Engineering, Chungbuk National University, Cheongju, Chungbuk 28644, Republic of Korea
Prof. G. D. Park
Department of Advanced Materials Engineering, Chungbuk National University, Chungdae-ro 1, Seowon-gu, Cheongju, Chungbuk 28644, Republic of Korea
The ORCID identification number(s) for the author(s) of this article can be found under https://doi.org/10.1002/eem2.70249.

DOI: 10.1002/eem2.70249

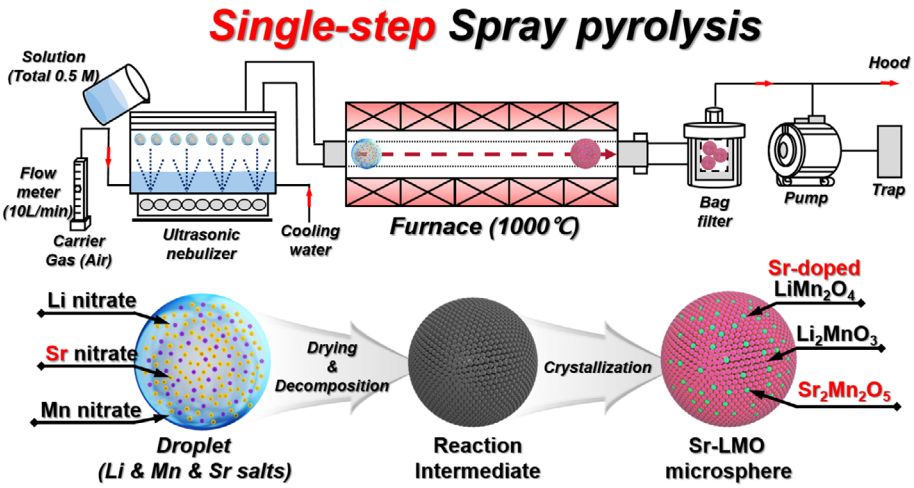

Scheme 1. Illustration of single-step spray pyrolysis method for multi-phase microspheres comprising Sr-doped $LiMn_2O_4$ spinel, a minor $Sr_2Mn_2O_5$ phase, and a C2/m layered Li_2MnO_3-like structure.

can reduce specific capacity if stoichiometry is not carefully controlled.[20–22] These limitations highlight the need for a rapid, scalable synthesis method capable of precise dopant incorporation and morphology control without sacrificing electrochemical performance.

Spray pyrolysis offers a single-step, inherently scalable pathway to composition-tunable cathode powders with uniform morphology.[23] Each aerosol droplet acts as a micro-reactor, converting within seconds into spherical secondary particles composed of nanoscale primary crystallites—an architecture that supports high tap density, short Li^+ diffusion lengths, and tunable porosity.[24–26] While this technique has shown promise for LMO, the synthesis-temperature window required to maximize intrinsic performance and its coupling to dopant chemistry, grain-boundary phases, and multi-phase interactions has remained comparatively underexplored.

In this work, we optimize the spray-pyrolysis temperature for LMO and then first introduce a single-step strontium-doping strategy to produce multi-phase microspheres comprising Sr-doped spinel $LiMn_2O_4$, a minor $Sr_2Mn_2O_5$ phase, and a C2/m layered Li_2MnO_3-like structure. The deliberate coexistence of these phases provides synergistic advantages: Sr doping increases the average Mn oxidation state, suppressing Jahn–Teller distortion and stabilizing the spinel lattice; $Sr_2Mn_2O_5$ refines grain boundaries and acts as a mechanical buffer against crack propagation; and the layered Li_2MnO_3-like domains enhance structural stability, diversify Li^+ diffusion pathways, and mitigate Mn dissolution and electrolyte side reactions. Electrochemical evaluation confirms that these composite cathodes deliver superior cycling stability and rate performance compared to LMO and commercial counterparts, demonstrating that combining process optimization and controlled multi-phase coexistence within a rapid spray-pyrolysis framework is a scalable route to robust, high-voltage spinel-based cathodes.

2. Results and Discussion

Scheme 1 illustrates the single-step synthesis principle of multi-phase microspheres comprising Sr-doped $LiMn_2O_4$ spinel, a minor $Sr_2Mn_2O_5$ phase, and a C2/m layered Li_2MnO_3-like structure *via* a spray pyrolysis process. This synthesis method integrates droplet generation, pyrolysis, and crystallization in a single thermal treatment system, enabling the direct formation of spherical multi-phase cathode powders without additional post-treatment steps. Such a process offers significant advantages in terms of efficiency and simplicity. The precursor solution was prepared by dissolving lithium nitrate, manganese nitrate hexahydrate, and strontium nitrate in distilled water with a Li:Mn:Sr molar ratio of 1:1.95:0.05. The solution was then converted into fine droplets using an ultrasonic nebulizer. These droplets were transported into the furnace chamber of 1200 mm by an air carrier gas at a flow rate of approximately 10 L min^{-1}. As the droplets entered the high-temperature region of the furnace, the solvent (distilled water) rapidly evaporated, followed by the thermal decomposition of the metal salt precursors. Through this rapid pyrolysis and subsequent crystallization, multi-phase microspheres comprising Sr-doped $LiMn_2O_4$ spinel, a minor $Sr_2Mn_2O_5$ phase, and a C2/m layered Li_2MnO_3-like structure (denoted as Sr-LMO) were directly obtained, completing the one-step formation of cathode powders.

Prior to the implementation of the Sr doping strategy, optimization of the synthesis temperature in the one-step spray pyrolysis process was conducted to establish the most favorable conditions for spinel cathode synthesis. To determine the optimal synthesis conditions, LMO cathode materials were synthesized *via* spray pyrolysis at controlled temperatures from 800 to 1100 °C. The corresponding structural and electrochemical data are provided in **Figure 1**a–h and Figures S1–S5, Supporting Information. XRD analysis confirmed the presence of the spinel $LiMn_2O_4$ structure (PDF #88-1030) in all specimens synthesized at 800, 900, 1000, and 1100 °C (Figure S1, Supporting Information). To investigate temperature-dependent variations in crystal structure, Rietveld refinement was performed, and the refined patterns and corresponding lattice parameters are shown in Figure 1a–d and Figure S2, Supporting Information. The lattice parameter increased steadily with synthesis temperatures from 800 to 1000 °C, indicating lattice expansion that can facilitate lithium-ion diffusion by increasing interplanar spacing. However, at 1100 °C, a notable contraction in the lattice parameter was observed, attributed to lithium volatilization at elevated temperatures.[27] The morphological evolution of the materials synthesized at different temperatures was examined *via* scanning electron microscopy (SEM), as shown in Figure 1e–h. In all cases, spherical secondary particles composed of aggregated primary crystallites were observed. Because the calcination temperature of 800 °C is relatively low, the sample exhibited the smallest primary particle size, indicating insufficient crystallization under these suboptimal conditions, which may hinder its electrochemical performance. To evaluate the electrochemical properties, all samples were assembled into half-cells and tested as cathodes in lithium-ion batteries. The galvanostatic charge–discharge profiles (Figure S4, Supporting Information) revealed that the 800 °C sample lacked the characteristic dual redox plateaus of $LiMn_2O_4$ and delivered the lowest initial discharge capacity (104.37 mA h g^{-1} at 0.1 °C), due to poor crystallinity. As the synthesis temperature increased, more defined Mn^{3+}/Mn^{4+} redox plateaus emerged,

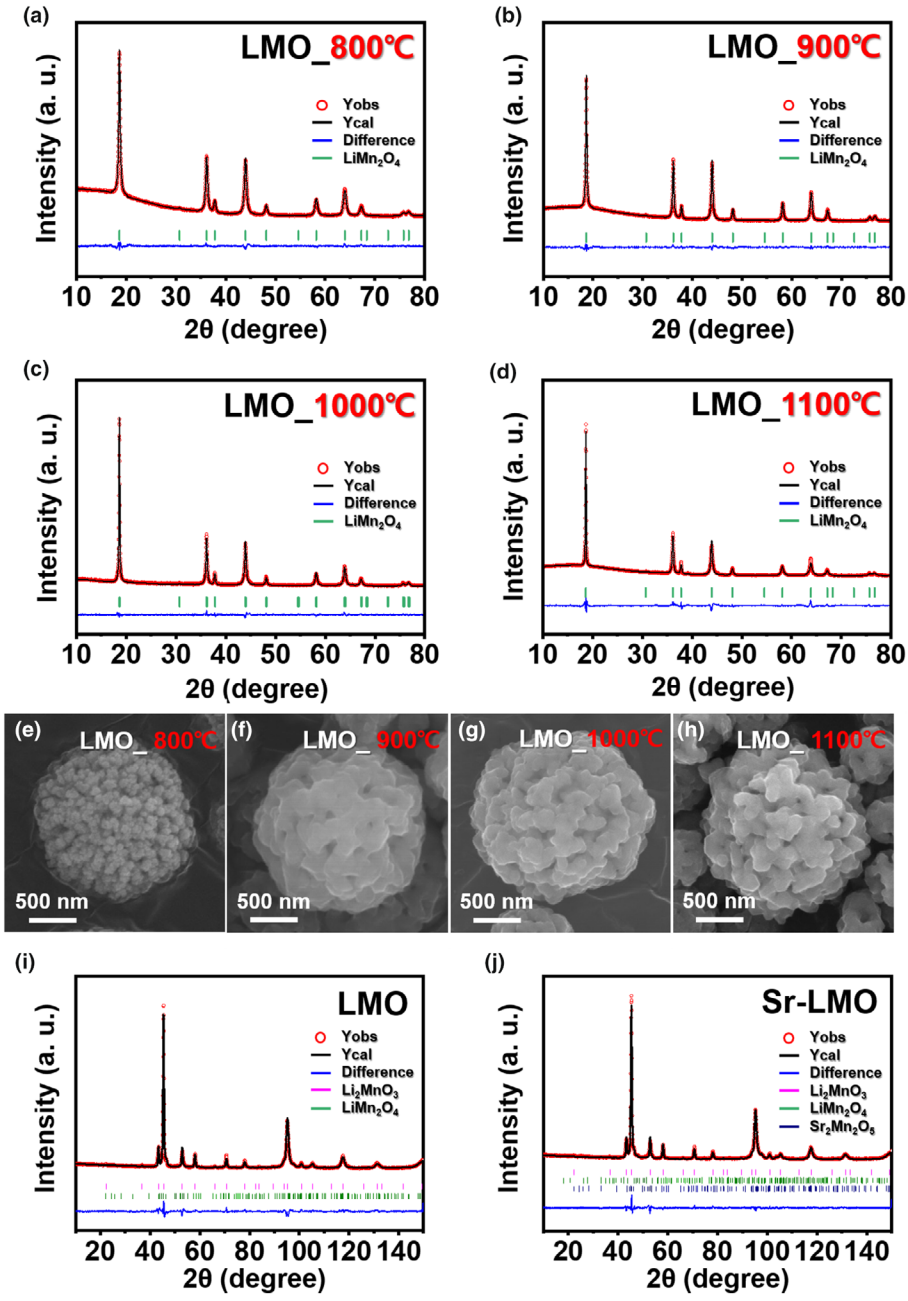

Figure 1. XRD refinement patterns, a) LMO_800 °C, b) LMO_900 °C, c) LMO_1000 °C, d) LMO_1100 °C, e–h) FE-SEM images at high magnifications of LMO synthesized at 800–1100 °C, and i, j) neutron diffraction refinements of LMO and Sr-LMO, respectively.

indicating improved structural ordering. Notably, the 1100 °C sample exhibited a decline in initial capacity, likely due to lithium loss during synthesis at high temperature. Among all, the sample synthesized at 1000 °C exhibited the highest lattice parameter, which is advantageous for Li^+ diffusion, and delivered the highest initial discharge capacity as well as superior rate capability and cycling performance (Figure S5, Supporting Information). Therefore, 1000 °C was identified as the optimal synthesis temperature, offering a favorable balance between crystallinity, structural integrity, and electrochemical performance for undoped LMO spinel cathodes.

After optimizing the synthesis temperature of $LiMn_2O_4$ at 1000 °C, we introduced a strontium-doping strategy under the same conditions to further enhance its electrochemical performance. Both LMO and Sr-LMO samples were then comprehensively analyzed using inductively coupled plasma optical emission spectroscopy (ICP-OES), X-ray diffraction (XRD), and neutron diffraction (ND) to investigate their structural characteristics. As presented in Table S1, Supporting Information, the compositions of LMO and Sr-LMO were quantitatively analyzed using ICP-OES. In the synthesis of LMO, a 5 wt% excess of lithium precursor was intentionally introduced to compensate for lithium volatilization that typically occurs during high-temperature reaction.[28,29] As a result, the molar ratio of Li to Mn was found to be approximately 1:2, confirming that the designed stoichiometry of $LiMn_2O_4$ was well maintained. In the case of Sr-LMO, the mole ratios of Li, Mn, and Sr were determined to be approximately 1:1.95:0.05, which is consistent with the targeted composition and verifies the successful incorporation of Sr into the spinel framework. As shown in Figures S6 and S7, Supporting Information, both samples exhibit XRD patterns consistent with the cubic spinel structure (space group Fd3-m). Upon Sr doping, a marginal lattice contraction was observed. Contrary to typical ionic radius considerations, this contraction is attributed to an increased proportion of Mn^{4+} in the lattice, which possesses a smaller ionic radius than Mn^{3+}.[30] The refined lattice parameter a decreased from 8.2378 Å (LMO) to 8.2368 Å (Sr-LMO), corresponding to a reduced unit cell volume from 559.03 $Å^3$ to 558.82 $Å^3$ (Table S2, Supporting Information). These changes suggest that Sr^{2+} ions were successfully incorporated into the lattice, leading to an increased proportion of Mn^{4+}. The higher Mn^{3+} content mitigates the Jahn–Teller distortion typically associated with Mn^{3+} ions, thereby enhancing the structural stability of the spinel framework during electrochemical cycling.

To gain deeper insight into atomic-level structure and site occupancy, neutron diffraction measurements were performed as shown in Figure 1i,j. Unlike XRD, which mainly confirmed the spinel $LiMn_2O_4$ phase, ND analysis further revealed the coexistence of Li_2MnO_3. Importantly, the Li_2MnO_3 phase provides additional Li^+ diffusion channels, thereby facilitating lithium transport and potentially improving electrochemical performance. The refined structural parameters are summarized in Tables S3–S5, Supporting Information. In the LMO sample, Mn

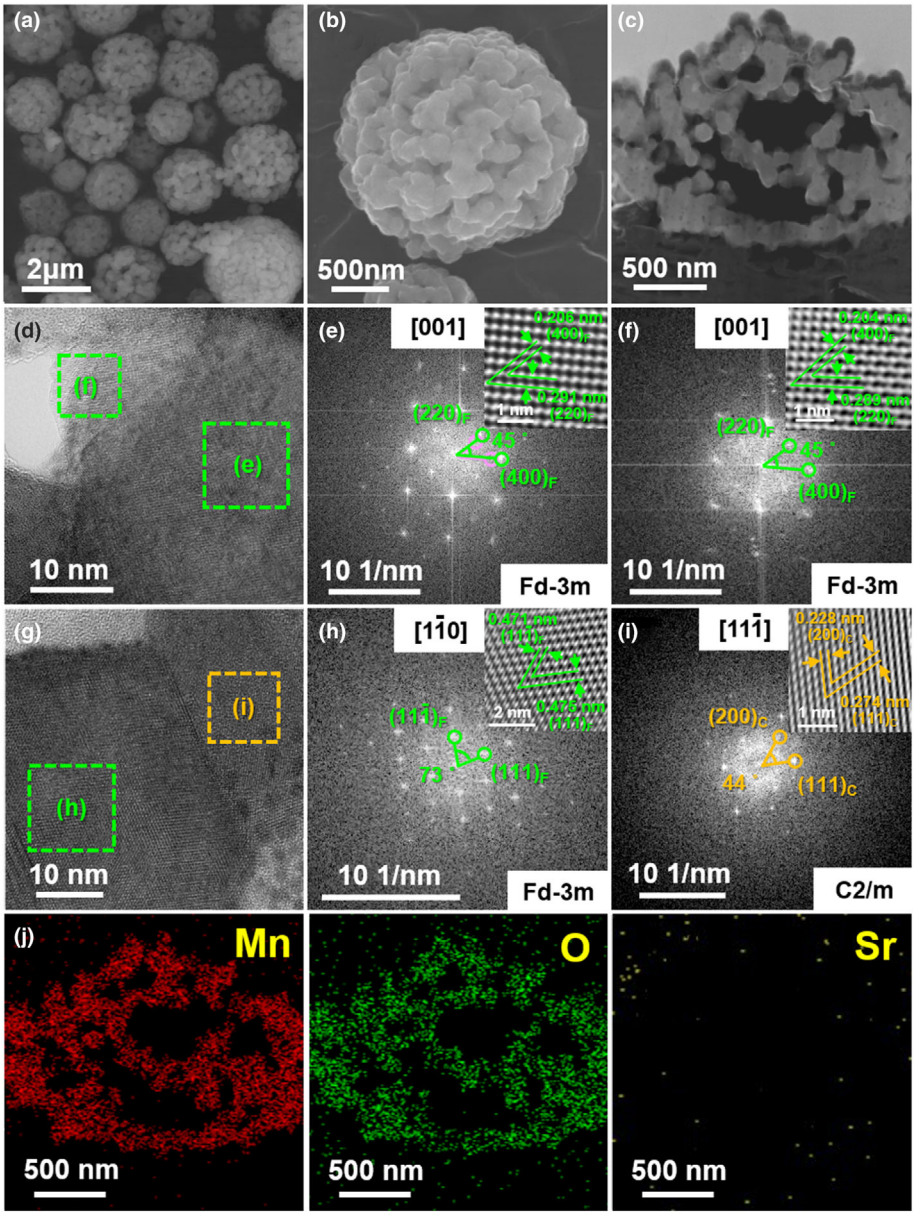

Figure 2. Morphological and structural characterizations of LMO: a, b) FE-SEM images at different magnifications, c) cross-sectional FE-SEM image after FIB processing, d, g) HR-TEM images, FFT diffraction pattern and corresponding IFFT image from the (e, f, h, and i) selected region, and j) elemental mapping images.

ions are predominantly located at the 16d sites with partial lithium occupancy at the 8a sites. Upon Sr doping, notable changes in site occupancy were observed. Specifically, the Mn–O bond length was found to decrease from 1.963 Å in LMO to 1.949 Å in Sr-LMO, consistent with the increase in Mn^{4+} content. This contraction of the Mn–O octahedra enhances structural robustness by reducing Jahn–Teller distortion associated with Mn^{3+}, and is expected to contribute to improved cycling stability. The suppression of local Jahn–Teller distortion by replacing Mn^{3+} with Sr^{2+} contributes to enhanced structural stability during cycling. In addition, the Li–O bond length increased from 1.961 Å in LMO to 1.987 Å in Sr-LMO, which can facilitate Li^+ mobility by lowering the migration barrier and thus contribute to faster lithium diffusion. These structural refinements clearly demonstrate the beneficial role of Sr doping in modifying the crystallographic environment of LMO. The resulting improved structural robustness is expected to enhance Li^+ diffusion and cycling stability, making Sr-LMO a promising candidate for advanced lithium-ion battery cathodes.

Field-emission scanning electron microscopy (FE-SEM) and transmission electron microscopy (TEM) were employed to investigate the structural properties of the LMO and Sr-LMO samples. As observed in the FE-SEM images of LMO (**Figure 2**a–c), the sample exhibits well-formed spherical secondary particles that are uniformly distributed within the size range of 2–3 μm. In particular, Figure 2b shows that the LMO sample is composed of relatively large primary particles with substantial voids between them, indicating poor inter-particle contact and a reduced effective contact area. For TEM analysis, specimens were fabricated using focused ion beam (FIB) techniques, and the cross-sectional morphology examined by FE-SEM in Figure 2c confirmed the presence of large primary particles. To elucidate the crystallographic structure, fast Fourier transform (FFT) patterns were obtained from regions within the particle interior and from the particle surface as indicated in Figure 2d, with the corresponding patterns shown in Figure 2e,f. Both the interior and surface regions exhibit distinct lattice fringes corresponding to the (220) and (400) planes, with measured d-spacing of 0.289 and 0.204 nm for the interior and 0.291 and 0.206 nm for the surface. These features confirm the successful synthesis of spinel-structured LMO. In addition, high-resolution TEM combined with FFT and IFFT analysis (Figure 2g–i) revealed the coexistence of cubic Fd3-m spinel and monoclinic C2/m domains. The region marked h in Figure 2g displayed diffraction spots indexed to the (111) and (11$\bar{1}$) planes, consistent with the cubic spinel framework, while the region marked i exhibited spots corresponding to the (200) and (111) planes, indicative of a local monoclinic C2/m ordering. These observations suggest that pristine LMO inherently contains both spinel and monoclinic domains, with the monoclinic regions acting as additional Li^+ diffusion pathways.

For the Sr-LMO sample, FE-SEM images in **Figure 3**a–c reveal spherical secondary particles of comparable size (2–3 μm) but composed of smaller primary particles with narrower voids between them compared to LMO. This morphology implies improved particle-to-particle contact and a larger interfacial area, which can be attributed to the influence of

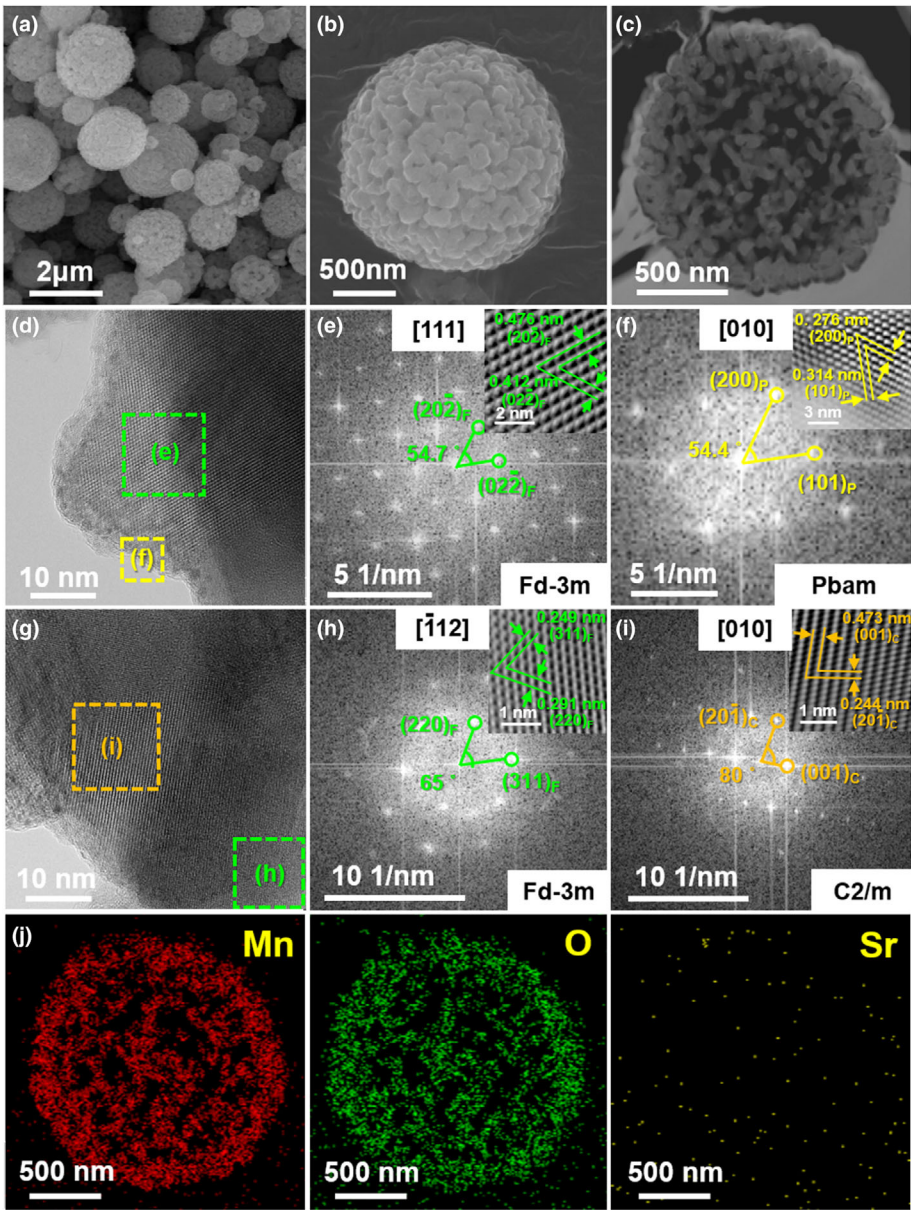

Figure 3. Morphological and structural characterizations of Sr-LMO: a, b) FE-SEM images at different magnifications, c) cross-sectional FE-SEM image after FIB processing, d, g) HR-TEM images, FFT diffraction pattern and corresponding IFFT image from the (e, f, h, and i) selected region, and j) elemental mapping images.

Sr doping on particle growth during synthesis. The cross-sectional morphology observed in Figure 3c further supports the reduced primary particle size. High-resolution TEM analysis, as shown in Figure 3d, provided additional insights into the local crystal structure. The FFT pattern obtained from the particle interior (Figure 3e) shows diffraction spots corresponding to the (20$\bar{2}$) and (02$\bar{2}$) planes along the [111] zone axis, confirming that the spinel LMO phase remains intact after Sr incorporation. By contrast, the FFT pattern collected from the particle surface (Figure 3f) reveals spots corresponding to the (200) and (101) planes, along with the formation of a surface-localized $Sr_2Mn_2O_5$ phase. This secondary phase plays a crucial role in suppressing the growth of primary particles, thereby contributing to the observed reduction in particle size. The microstructural observations in Figure 3g–i confirmed the coexistence of cubic spinel and monoclinic C2/m domains in Sr-LMO, similar to LMO. The region marked h in Figure 3g exhibited diffraction spots indexed to the (311) and (220) planes, consistent with the cubic spinel structure, whereas the region marked i revealed diffraction spots corresponding to the (001) and (20$\bar{1}$) planes, indicating monoclinic ordering at the particle surface. These findings highlight that the formation of a surface $Sr_2Mn_2O_5$ phase reduces the size of primary particles and enhances structural robustness. At the same time, Sr doping mitigates Jahn–Teller distortion by modulating manganese oxidation states. Collectively, these two effects reinforce both the electrochemical stability and the structural integrity of the spinel LMO system.

To investigate the chemical states of the cathode materials and elucidate changes in the manganese oxidation states upon doping, X-ray photoelectron spectroscopy (XPS) analysis was conducted, and the corresponding spectra for the Mn 2p, Mn 3 s, and Sr 3d regions are presented in **Figure 4**. Figure 4a,b present the Mn 2p spectra of LMO and Sr-LMO, respectively, where the Mn 2p peak is split into Mn $2p_{1/2}$ and Mn $2p_{3/2}$ components due to spin–orbit coupling, located at binding energies of 654.44 and 642.91 eV.[31,32] Notably, both the Mn $2p_{1/2}$ and Mn $2p_{3/2}$ peaks exhibit characteristic splitting corresponding to Mn^{3+} and Mn^{4+} oxidation states, and peak area analysis revealed an increase in the Mn^{4+}/Mn^{3+} ratio from 1.08 to 1.71 following Sr doping. The variation in Mn oxidation states (ΔE) can also be corroborated by the splitting of the Mn 3 s peak into two distinct components (Figure 4c,d), located at 89.9 and 84.9 eV, from which the average oxidation state (AOS = 8.956–1.126 ΔE) of Mn was calculated using an empirical relationship.[33,34] The results show an increase in the average Mn oxidation state from 3.42 in LMO to 3.63 in Sr-LMO, indicating the oxidation enhancement arising from Sr incorporation as well as the slight increase in the mass fraction of the monoclinic C2/m Li_2MnO_3 phase, which provides additional Li^+ diffusion channels, thereby facilitating lithium transport and potentially enhancing electrochemical performance, as listed in Tables S3, S4, Supporting Information. Figure 4e,f display the Sr 3d spectrum, where the Sr $3d_{3/2}$ and Sr $3d_{5/2}$ peaks are located at 135.69 and 133.92 eV, respectively, providing clear evidence of the successful incorporation of Sr into the LMO lattice, and this incorporation is associated with a reduction in the Mn^{3+} fraction and an increase in the average Mn oxidation state, which are expected to

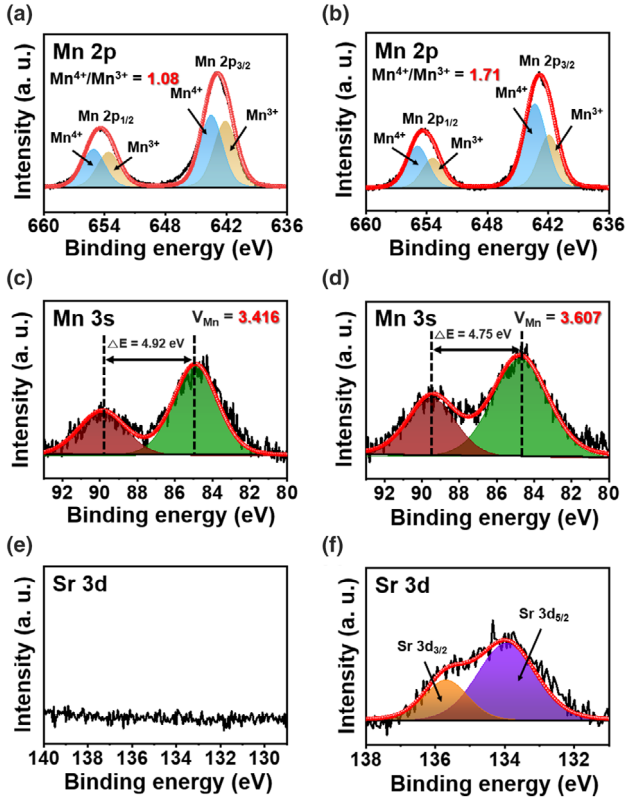

Figure 4. XPS narrow-scan spectra of the LMO sample; a) Mn 2p, b) Mn 3 s, and c) Sr 3d, and Sr-LMO sample; d) Mn 2p, e) Mn 3 s, and f) Sr 3d.

effectively mitigate the Jahn–Teller distortion and enhance the structural stability of the spinel framework.[35,36] To further confirm the spatial distribution of Sr and the uniformity of Mn oxidation states, XPS depth profiling was carried out for LMO and Sr-LMO at sputtering depths of surface, 50, 100, and 200 nm (Figures S8 and S9, Supporting Information). Figure S9a, Supporting Information shows Sr 3d spectra with consistent peak positions and intensities across all sputtering depths, alongside Mn 2p and Mn 3 s spectra that indicate nearly identical Mn oxidation states, demonstrating that the chemical environment of Mn reflects the uniform distribution of Sr throughout the particles. This uniform elemental distribution is attributed to the spray pyrolysis synthesis route, in which Sr precursors are introduced into the spray solution, ensuring atomic scale homogeneity during particle formation. Consequently, both the Sr content and Mn^{4+}/Mn^{3+} ratio remain consistent across different depths, confirming the uniform doping characteristics of Sr-LMO.

The electrochemical characteristics of the fabricated cathodes were evaluated through coin cell testing, and the results are shown in **Figure 5**. Figure 5a,b display the galvanostatic charge/discharge profiles for LMO and Sr-LMO samples tested at 0.1 C (1 C = 148 mA h g^{-1}) within the range of 3.2–4.3 V. LMO and Sr-LMO electrodes present obvious plateaus, showing that the insertion and extraction process of Li^+ are performed in two steps.[37,38] Additionally, the Li_2MnO_3 phase, present in minor amounts, remains electrochemically inactive within this voltage range and therefore does not contribute additional plateaus.[39] The LMO electrode has a larger initial discharge capacity than the Sr-LMO electrode, likely due to the formation of $Sr_2Mn_2O_5$, which was electrochemically inactive in LIBs. Figure 5c presents the

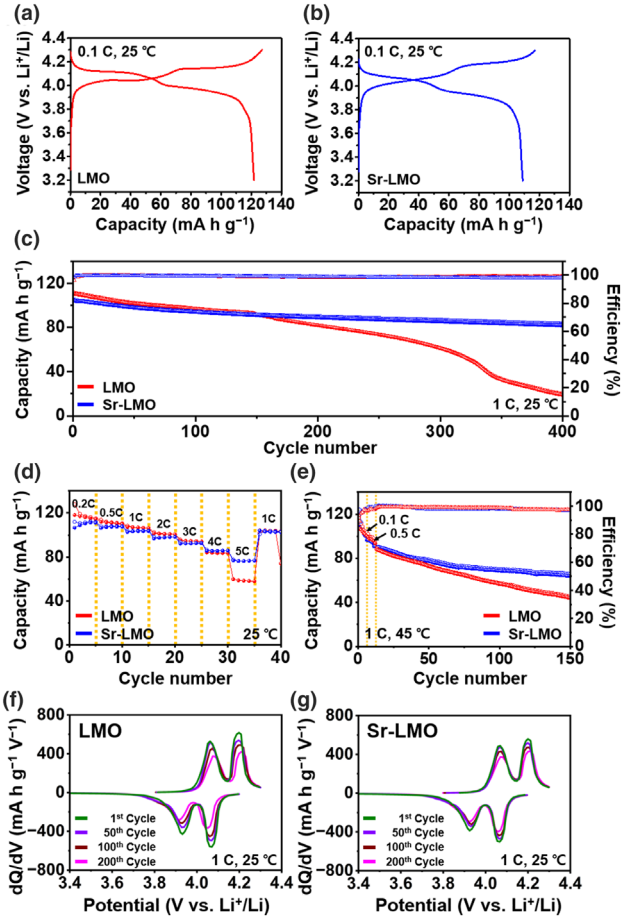

Figure 5. Electrochemical performance of LMO and Sr-LMO: a, b) charge–discharge profiles at 0.1 C, c) cycle performance at 1 C and 25 °C, d) rate capability at various current densities, e) cycling stability at 1 C under elevated temperature (45 °C), and f, g) dQ/dV curves of LMO and Sr-LMO during 200 cycles, respectively.

cycling performances of LMO and Sr-LMO during 400 cycles at 1 C. During the initial discharge, the capacities of LMO and Sr-LMO are 88.67 and 88.06 mA h g^{-1}, respectively, indicating the presence of inactive components, as shown in the general profile. However, after repeated cycling, the capacity trend reverses, and after 400 cycles, the capacity retention ratios of LMO and Sr-LMO are 19.2% and 51.3%, respectively, demonstrating that Sr doping leads to enhanced long-term capacity retention. These electrochemical results clearly indicate that the Sr-LMO cathode delivers enhanced performance compared with previously reported $LiMn_2O_4$ based cathodes (Table S6, Supporting Information). This enhanced cycling performance arises from the ability of Sr incorporation to mitigate Jahn–Teller distortion associated with Mn^{3+}, thereby stabilizing the spinel lattice. Furthermore, the slightly increased proportion of Li_2MnO_3 in Sr-LMO, as indicated by neutron diffraction analysis, helps suppress Mn dissolution while providing additional Li^+ diffusion pathways, collectively contributing to the observed improvement in capacity retention.[40,41] Figure 5d shows the discharge capacities of LMO and Sr-LMO electrodes under continuous cycling at different current rates. The Sr-LMO electrode exhibits much better discharge capacity than LMO at high rate. The Sr-modified electrode shows much improved rate capability compared with the bare LMO,

demonstrating the highest performance at 5 C. As the rate increases from 0.1 C to 5 C, the LMO electrode shows discharge capacity retention of 71.9% at 5 C; conversely, the Sr-LMO electrode maintains a reversible discharge capacity retention of 50.3%. Under high-rate cycling, the local accumulation of excess Li^+ in LMO can induce structural distortion, potentially transforming the cubic phase into the tetragonal phase.[42] The enhanced rate capability of Sr-LMO arises from the incorporation of Sr, which increases the Mn^{4+} content and helps suppress Jahn–Teller distortion and Mn^{3+} disproportionation, synergistically contributing to enhanced Li^+ diffusion due to the slightly higher proportion of Li_2MnO_3 present within the composite.[43] The combined effect stabilizes the spinel lattice and provides additional Li^+ diffusion pathways, collectively contributing to the superior high-rate performance of Sr-LMO. To estimate cycling stability at elevated temperature, which is one of the most important reasons inhibiting the development of spinel cathodes, LMO and Sr-LMO electrodes are measured in 3.2–4.3 V at 45 °C (Figure 5e). For the first cycle at 1 C, the discharge capacity of LMO and Sr-LMO electrodes are 87.8 and 90.85 mA h g^{-1}, respectively. After 150 cycles, the capacity retention ratios of the LMO and Sr-LMO electrodes are about 50.3% to 70.4%. This demonstrates that the addition of Sr has contributed to improved cycling stability due to an increased ratio of Mn^{4+} ions and miniaturized primary particle size, which suppresses structural collapses. Figure 5f,g show differential discharge capacity vs. voltage (dQ/dV) profiles of LMO and Sr-LMO measured after different cycles at a rate of 1 C, exhibiting four redox peaks during both charge and discharge, which correspond to the Mn^{3+}/Mn^{4+} redox reactions of the spinel LMO. No additional peaks associated with Li_2MnO_3 activation are observed, confirming that these domains are electrochemically inactive within this voltage range. For the LMO electrode (Figure 5f), the reduction peaks shift obviously to lower potentials, and the oxidation peaks shift to higher potentials. Also, the peak intensity rapidly decreases with cycling, mainly due to Mn dissolution and severe structural degradation.[44] In contrast, Sr-LMO exhibits enhanced electrochemical stability compared to LMO, as indicated by only minor shifts in redox peak potentials after 200 cycles. Furthermore, the fading of peak intensity occurs at a significantly slower rate compared to the LMO electrode, suggesting improved structural integrity and interfacial stability during prolonged cycling. Although Li_2MnO_3-like domains are inactive, their slightly higher abundance in Sr-LMO forms local spinel–layered interfaces that provide additional Li^+ diffusion channels, while $Sr_2Mn_2O_5$ suppresses Mn^{3+} distortion and alleviates lattice strain, collectively contributing to improved cycling stability.

To further illustrate the reason for the improved cycle stability and rate capability, EIS were performed for the LMO and Sr-LMO at fresh and after 200 cycles at 1 C (**Figure 6**a,b). The EIS spectra typically consist of four components: R_s (solution resistance), R_{sei} (resistance of the solid electrolyte interphase), R_{ct} (charge transfer resistance), and W (Warburg impedance related to lithium-ion diffusion). Before cycling, the spectra exhibit a single semicircle in the high-frequency region, corresponding to R_s and R_{ct}.[45,46] However, after 200 cycles, two distinct semicircles are observed at the high and medium frequencies due to the formation of a SEI layer, which introduces an additional resistance (R_{sei}).[47] To quantitatively analyze the electrochemical behavior and reaction kinetics, we fitted the EIS spectra using an equivalent circuit model as illustrated in Figure S10, Supporting Information. As shown in Table S6, the LMO electrode exhibited an R_{ct} of 126.17 Ω and a diffusion coefficient (D_{Li+}) of 8.29E-13 cm^2 s^{-1}. Also, the Sr-LMO showed a similar R_{ct} of 133.32 Ω, with D_{Li+} of 1.04E-12 cm^2 s^{-1}, indicating that Sr doping has little impact on the charge transfer kinetics and diffusion at the initial state. However, after 200 cycles, Sr-LMO showed a reduced R_{ct} of 56.17 Ω and R_{sei} of 21.03 Ω, along with a higher D_{Li+} of 7.99E-13 cm^2 s^{-1}. On the other hand, LMO exhibited a higher R_{ct} of 68.4 Ω, R_{sei} of 47.11 Ω, and a lower D_{Li+} of 5.53E-14 cm^2 s^{-1}. The higher lithium diffusion coefficient in Sr-LMO can be attributed to the increased fraction of Li_2MnO_3 within the composite, which provides additional Li^+ diffusion pathways.[48] Moreover, the Sr doping effectively suppresses Jahn–Teller distortion during cycling, preventing structural distortions and allowing the Li^+ diffusion channels to be maintained.[49] This result indicates that Sr modification effectively suppresses the collapse of crystallinity and degradation of the electronic conductivity of the SEI layer caused by Mn dissolution during cycling. Consequently, the Sr-LMO electrode demonstrated that Sr modification enhanced cycle life span and cycling stability. To evaluate the degree of micro-crack formation induced by prolonged cycling, top-view FE-SEM imaging was performed on the electrodes after 200 cycles. As shown in Figure 6c,d, the cycled LMO electrode exhibited pronounced micro-cracks along the grain boundaries of the primary particles, indicating structural degradation and particle detachment accelerated by repeated cycling. In contrast, the Sr-LMO electrode, as depicted in Figure 6c, retained an intact primary particle structure with minimal evidence of micro-crack formation. This enhanced structural stability is attributed to the formation of $Sr_2Mn_2O_5$ at the grain boundaries, which alleviates mechanical stress, along with the slightly increased fraction of Li_2MnO_3 within the composite, providing additional Li^+ diffusion pathways that suppress side reactions.[50,51] Furthermore, Sr doping inhibits Mn dissolution during cycling, preventing structural collapse. Collectively, these effects maintain the integrity of the electrode microstructure, consistent with the observed long-term cycle stability and enhanced capacity retention. **Figure 7** presents the XPS spectra of the electrode surfaces after 200 cycles, focusing on the chemical bonding environments of F 1s and Mn 2p. In Figure 7a,c, both LMO and Sr-LMO electrodes exhibit two characteristic

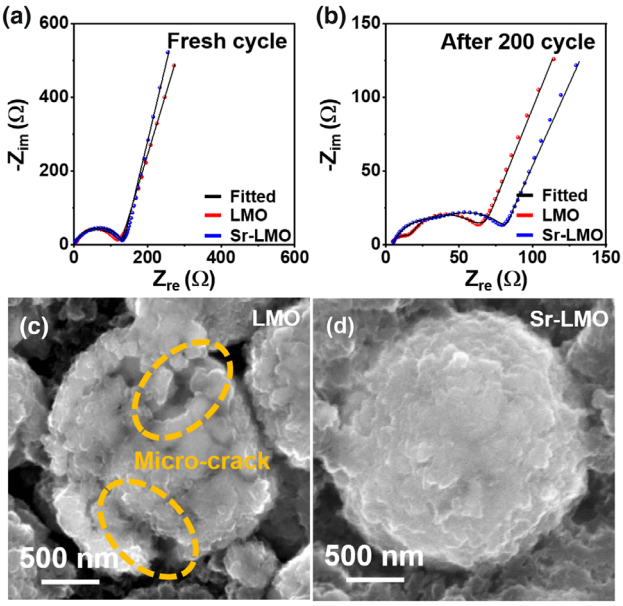

Figure 6. EIS spectra of LMO and Sr-LMO electrodes measured a) in fresh cells and b) after the 200th cycle, and FE-SEM images of the electrodes after 200 cycles: c) LMO and d) Sr-LMO.

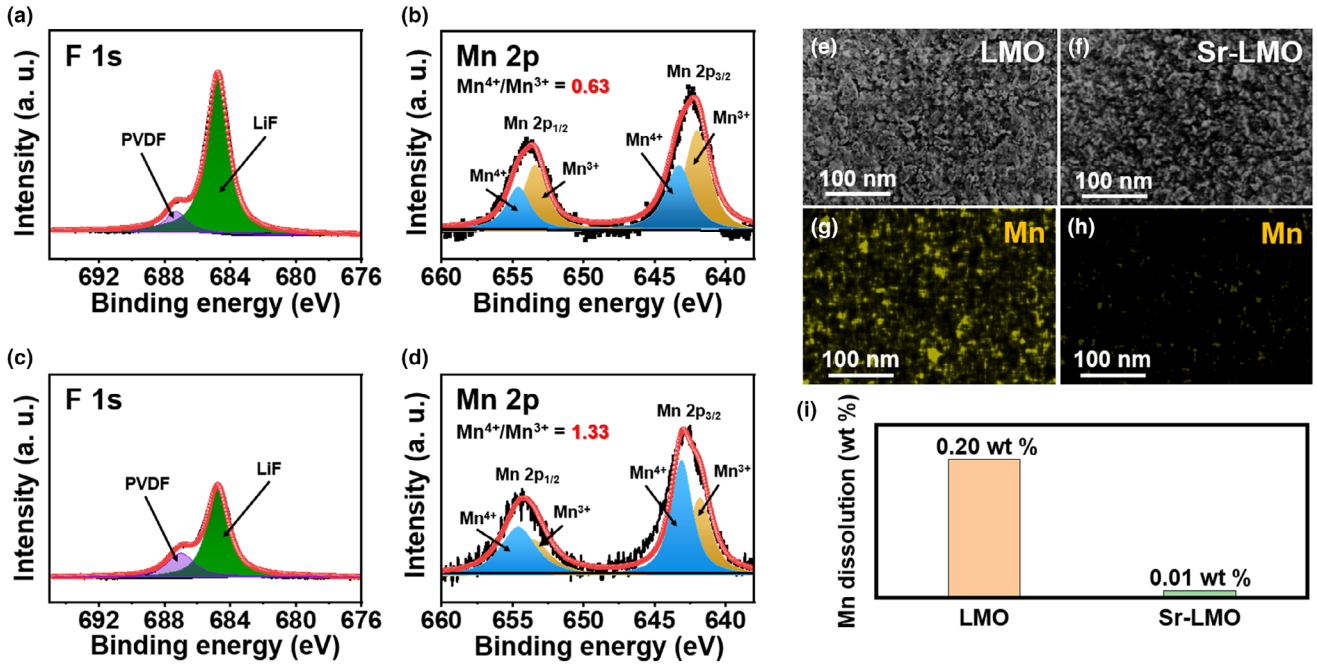

Figure 7. Post-cycling analyses: XPS narrow-scan spectra after 200 cycles for a, b) LMO (F 1s and Mn 2p) and c, d) Sr-LMO (F 1s and Mn 2p); e, f) FE-SEM images of graphite electrodes after 200 cycles in full cells with LMO and Sr-LMO, respectively; g, h) Mn elemental mapping of graphite electrodes coupled with LMO and Sr-LMO; and i) Mn mass concentration obtained from EDS analysis.

peaks in the F 1s region after repeated cycling. The peak at 687.30 eV corresponds to the P–F bonds associated with the PVDF binder and $LiPF_6$, while the peak at 684.75 eV is attributed to LiF.[52] Notably, the LMO electrode displays a more intense LiF-related peak compared to Sr-LMO. Since LiF is an electrochemically inactive and insoluble impurity that hinders Li^+ diffusion and contributes to capacity fading, its higher accumulation in LMO suggests a major factor behind its inferior cycling stability.[53] Figure 7b,d show the Mn 2p spectra of LMO and Sr-LMO electrodes, respectively, revealing the relative ratios of Mn^{3+} and Mn^{4+} species.[54,55] The Sr-LMO electrode maintained a lower Mn^{3+} content even after prolonged cycling, which can be explained by the combined effects of Sr doping, the higher fraction of Li_2MnO_3 within the composite, and the presence of $Sr_2Mn_2O_5$ at the grain boundaries. Sr doping stabilizes the Mn oxidation states and suppresses Jahn–Teller distortion, Li_2MnO_3 provides additional Li^+ diffusion pathways that mitigate structural distortion, and $Sr_2Mn_2O_5$ prevents microcrack formation, suppresses side reactions, and inhibits Mn dissolution. These factors collectively maintain structural integrity and contribute to the superior long-term cycling stability of Sr-LMO. To quantitatively evaluate the extent of Mn dissolution and subsequent deposition on the anode, full cells were assembled using LMO and Sr-LMO as cathodes with graphite anodes. During cycling, Mn^{3+} ions in LMO are prone to disproportionation at elevated potentials:[56]

$$2Mn^{3+} \rightarrow Mn^{4+}(\text{insoluble}) + Mn^{2+}(\text{soluble}), \quad (1)$$

where insoluble Mn^{4+} remains in the cathode, while soluble Mn^{2+} dissolves into the electrolyte. This dissolution is further promoted by HF generated via $LiPF_6$ hydrolysis:[57,58]

$$LiPF_6 + H_2O \rightarrow LiF + POF_3 + 2HF, \quad (2)$$

$$2LiMn_2O_4 + 4H^+ \rightarrow 3MnO_2 + Li^+ + Mn^{2+} + 2H_2O \quad (3)$$

The dissolved Mn^{2+} species then migrate toward the graphite anode and are reduced on the surface:[59]

$$Mn^{2+} + 2e^- \rightarrow Mn \quad (4)$$

After 200 cycles at 1 C, the graphite electrodes were harvested and subjected to EDS mapping analysis to confirm Mn deposition on the anode surface (Figure 7e–i). As shown in Figure 7i, the LMO cell exhibited a significantly higher Mn content of 0.20 wt %, whereas the Sr-LMO showed a markedly lower value of 0.01 wt %. This result clearly demonstrates that Sr doping effectively suppresses Mn dissolution from the cathode, and the presence of $Sr_2Mn_2O_5$ further contributes by inhibiting side reactions with the electrolyte that can accelerate Mn migration. The improved chemical stability is attributed to the reduced presence of unstable Mn^{3+} species and the suppression of Jahn–Teller distortion, which commonly accelerates structural degradation and Mn^{2+} migration.[60] Therefore, Sr modification plays a key role in maintaining cathode integrity and minimizing transition metal crossover, contributing to enhanced long-term cycling stability.

To thoroughly evaluate the commercial applicability of the Sr-LMO electrode, pouch-type full-cell electrochemical performance tests were conducted as shown in **Figure 8**. The synthesized Sr-LMO was employed as the cathode, while graphite was used as the anode. For comparison, a full cell was also assembled under identical conditions using commercial LMO (denoted as c-LMO) as the cathode material. Prior to the electrochemical test, the structural and morphological properties of the c-LMO were characterized in Figures S13 and S14, Supporting Information. XRD analysis confirmed that c-LMO exhibits a cubic spinel structure (space group Fd3-m) similar to that of the synthesized LMO, while SEM images

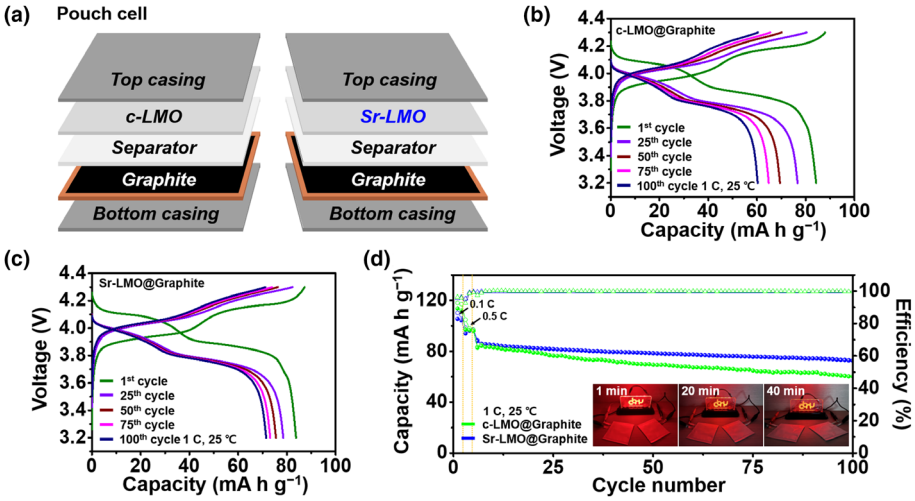

Figure 8. Electrochemical characterization of pouch-type full cells; a) schematic illustration of the fabricated pouch-cell configurations with c-LMO and Sr-LMO cathodes, charge–discharge profile of b) c-LMO@graphite full cell, and c) Sr-LMO@graphite full cell, d) cycling performance of c-LMO@graphite and Sr-LMO@graphite full cells at 1 C (inset: an 8 V LED glowing for 40 min, verifying device operability).

revealed the particle morphology and size distribution of c-LMO. Figure 8a schematically illustrates the assembly of Sr-LMO@graphite and c-LMO@graphite pouch cells, and the full cells were tested for cycling stability at 1 C within a voltage range of 3.2–4.3 V. As shown in Figure 8b,c, the initial discharge capacities of the Sr-LMO@graphite and c-LMO@graphite cells were 85.86 and 85.13 mA h g^{-1}, respectively. After 50 cycles, the discharge capacities were 78.37 and 69.44 mA h g^{-1}, and at the 100th cycle, Sr-LMO@graphite maintained 72.58 mA h g^{-1}, while the c-LMO@graphite cell dropped to 60.21 mA h g^{-1}. These results correspond to capacity retentions of 84.53% and 70.73% for Sr-LMO and c-LMO, respectively, clearly demonstrating the superior cycling stability of Sr-LMO. The enhanced performance of Sr-LMO is attributed to improved structural integrity and electrochemical stability achieved through Sr doping. Furthermore, the practical applicability of the pouch cells was demonstrated by powering an 8 V LED for 40 min, as shown in the inset of Figure 8d, highlighting the reliable energy output of the Sr-LMO-based device. This indicates that Sr-LMO is a promising cathode candidate with high potential for commercial application, especially when paired with widely used graphite anodes.

3. Conclusion

In summary, a rapid, single-step spray pyrolysis method was successfully developed to synthesize multi-phase microspheres composed of Sr-doped $LiMn_2O_4$ spinel, minor $Sr_2Mn_2O_5$, and C2/m Li_2MnO_3-like domains directly from a single precursor solution without post-treatment. Careful temperature optimization identified 1000 °C as the most favorable condition for achieving high crystallinity, optimal lattice expansion, and superior electrochemical behavior in undoped LMO. The incorporation of Sr uniformly into the spinel lattice increased the Mn^{4+}/Mn^{3+} ratio, suppressed Jahn–Teller distortion, and refined particle morphology by forming surface-localized $Sr_2Mn_2O_5$. Neutron diffraction confirmed the presence of Li_2MnO_3-like regions, which diversified Li^+ diffusion pathways and stabilized the structural framework. Electrochemical testing showed that these features collectively improved cycling stability, rate performance, and thermal durability. Sr-LMO retained 81.72 mA h g^{-1} after 400 cycles at 1 C and delivered superior capacity at 5 C compared to pristine and commercial LMO. Elevated-temperature cycling verified reduced Mn dissolution, and pouch-cell tests with graphite anodes confirmed higher capacity retention and reliable power delivery. These results highlight one-pot spray pyrolysis as a scalable, energy-efficient strategy for producing robust, high-voltage spinel cathodes. By uniting Sr doping, controlled multi-phase coexistence, and rapid aerosol processing in a single step, this approach offers strong potential for next-generation fast-charging lithium-ion batteries.

4. Experimental Section

LMO and Sr-LMO microspheres were synthesized via a single-step spray pyrolysis method. The spray solution for LMO was prepared by dissolving lithium nitrate ($LiNO_3$, 99%; Samchun) and manganese nitrate tetrahydrate ($Mn(NO_3)_2{\cdot}4H_2O$, 97%; Junsei) in 1 L of distilled water, maintaining a total metal ion concentration of 0.5 M with a Li:Mn molar ratio of 1:2. For Sr-LMO, the solution was similarly prepared with a Li:Mn:Sr molar ratio of 1:1.95:0.05, using strontium nitrate ($Sr(NO_3)_2$, 99%; Sigma-Aldrich) as the Sr source. In the synthesis of LMO, a 5 wt% excess of lithium precursor was intentionally introduced to compensate for lithium volatilization that typically occurs during high-temperature reactions. The precursor solution was atomized using a 1.7 MHz ultrasonic spray generator and carried into a quartz tube reactor (1200 mm length, 50 mm diameter) maintained at 1000 °C. Air was used as the carrier gas at a flow rate of 10 L min^{-1}. The resulting powders were collected without any further post-treatment. Detailed information pertaining to the characterization, electrochemical measurements, and computational methods of the prepared samples is provided in Supporting Information.

Acknowledgments

This work was supported by the National Research Foundation of Korea (NRF) grant funded by the Korea government (MSIT) (No. RS-2023-00217581). This work was supported by the Commercialization Promotion Agency for R&D Outcomes (COMPA) grant funded by the Korean Government (the Ministry of Science and ICT) (RS-2023-00304768). This research was supported by Chungcheongbuk-do Province and Convergence and Open Sharing System (COSS) Development Project (2025).

Conflict of Interest

The authors declare no conflict of interest.

Data Availability Statement

The data that support the findings of this study are available from the corresponding author upon reasonable request.

Supporting Information

Supporting Information is available from the Wiley Online Library or from the author.

Keywords

heteroatom doping, lithium manganese oxide, lithium-ion batteries, single process, spray pyrolysis

Received: September 23, 2025
Revised: November 5, 2025
Published online: November 27, 2025

[1] T.-F. Yi, Y.-R. Zhu, X.-D. Zhu, J. Shu, C.-B. Yue, A.-N. Zhou, *Ionics* **2009**, *15*, 779.
[2] M. Baazizi, M. Karbak, M. Aqil, S. Sayah, M. Dahbi, F. Ghamouss, *ACS Appl. Mater. Interfaces* **2023**, *15*, 40385.
[3] B. Rani, J. K. Yadav, P. Saini, A. Dixit, *Sustain. Energy Fuels* **2025**, *9*, 4262.
[4] G. Xu, Z. Liu, C. Zhang, G. Cui, L. Chen, *J. Mater. Chem. A* **2015**, *3*, 4092.
[5] X. Tang, J. Zhou, M. Bai, W. Wu, S. Li, Y. Ma, *J. Mater. Chem. A* **2019**, *7*, 13364.
[6] G. Ceder, A. Van der Ven, C. Marianetti, D. Morgan, *Model. Simul. Mater. Sci. Eng.* **2000**, *8*, 311.
[7] S. Zhang, H. Chen, J. Chen, S. Yin, Y. Mei, L. Ni, A. Di, W. Deng, G. Zou, H. Hou, *J. Energy Chem.* **2022**, *72*, 379.
[8] O. K. Park, Y. Cho, S. Lee, H.-C. Yoo, H.-K. Song, J. Cho, *Energy Environ. Sci.* **2011**, *4*, 1621.
[9] A. B. Haruna, D. H. Barrett, C. B. Rodella, R. M. Erasmus, A. M. Venter, Z. N. Sentsho, K. I. Ozoemena, *Electrochim. Acta* **2022**, *426*, 140786.
[10] N. Hellar, Y. Iwai, M. Ohzu, S. Brox, A. Dorai, R. Takekawa, N. Kuwata, J. Kawamura, M. Winter, *Commun. Mater.* **2025**, *6*, 23.
[11] B. Li, M. Wang, Y. Zhang, Q. Guo, R.-N. Tian, J. Chen, D. Wang, C. Dong, Z. Mao, *Electrochim. Acta* **2023**, *464*, 142898.
[12] W. Zeng, F. Xia, J. Wang, J. Yang, H. Peng, W. Shu, Q. Li, H. Wang, G. Wang, S. Mu, *Nat. Commun.* **2024**, *15*, 7371.
[13] Q. Wei, X. Wang, X. Yang, B. Ju, B. Hu, H. Shu, W. Wen, M. Zhou, Y. Song, H. Wu, *J. Mater. Chem. A* **2013**, *1*, 4010.
[14] X. Liang, S. Zeng, Y. Liu, L. Shi, T. Liu, *Mater. Sci. Technol.* **2015**, *31*, 443.
[15] Y. Shu, J. Zeng, J. Huang, G. Hu, K. Du, Z. Peng, Y. B. Cao, *ChemSusChem* **2021**, *14*, 5476.
[16] D. Zhan, F. Yang, Q. Zhang, X. Hu, T. Peng, *Electrochim. Acta* **2014**, *129*, 364.
[17] H. Chan, J. Duh, S. Sheen, *J. Power Sources* **2003**, *115*, 110.
[18] J. Yang, X. Shang, B. Hu, B. Zhang, Y. Wang, J. Yang, J. Liu, *J. Solid State Electrochem.* **2023**, *27*, 2029.
[19] P. Chand, V. Bansal, S. Lal, A. Joshi, Sukriti, A. Kumar, *J. Mater. Sci. Mater. Electron.* **2021**, *32*, 6648.
[20] Y. Zhang, H. Xie, H. Jin, X. Li, Q. Zhang, Y. Li, K. Li, F. Luo, W. Li, C. Li, *ACS Omega* **2021**, *6*, 21304.
[21] S. Zhang, W. Deng, R. Momen, S. Yin, J. Chen, A. Massoudi, G. Zou, H. Hou, W. Deng, X. Ji, *J. Mater. Chem. A* **2021**, *9*, 21532.
[22] Y. Deng, S. Wang, Y. Zhou, Y. Qian, X. Qin, G. Chen, *J. Appl. Electrochem.* **2018**, *48*, 1083.
[23] J. K. Kim, S. Y. Jeong, S. H. Lim, J. H. Oh, S. K. Park, J. S. Cho, Y. C. Kang, *Chem. Asian J.* **2019**, *14*, 3127.
[24] C. M. Sim, S. H. Choi, Y. C. Kang, *Chem. Commun.* **2013**, *49*, 5978.
[25] I. Taniguchi, C. Lim, D. Song, M. Wakihara, *Solid State Ionics* **2002**, *146*, 239.
[26] I. Taniguchi, K. Matsuda, H. Furubayashi, S. Nakajima, *AICHE J.* **2006**, *52*, 2413.
[27] Y. Huang, R. Jiang, S.-J. Bao, Y. Cao, D. Jia, *Nanoscale Res. Lett.* **2009**, *4*, 353.
[28] A. Manthiram, *Nat. Commun.* **2020**, *11*, 1550.
[29] X. Fang, M. Ge, J. Rong, C. Zhou, *ACS Nano* **2014**, *8*, 4876.
[30] P. Li, S. Luo, Y. Wang, J. Feng, L. Zhang, S. Yan, H. Li, Y. Tian, F. Teng, Q. Wang, A. He, F. Zhuge, *Energy Fuel* **2022**, *36*, 9329.
[31] Y. Zhang, P. Dong, M. Zhang, X. Sun, X. Yu, J. Song, Q. Meng, X. Li, Y. Zhang, *J. Appl. Electrochem.* **2018**, *48*, 135.
[32] J. Chen, N. Zhao, J. Zhao, J. Li, F.-F. Guo, G.-D. Li, *J. Solid State Electrochem.* **2018**, *22*, 331.
[33] H. Li, L. Xue, M. Ni, S. V. Savilov, S. M. Aldoshin, H. Xia, *Electrochem. Commun.* **2022**, *137*, 107266.
[34] Y. Pan, W. Jiawei, W. Haifeng, W. Song, Y. Chunyuan, H. Yue, *Nanoscale Adv.* **2023**, *5*, 3396.
[35] X. Zi, X. Huang, J. Song, H. Wu, J. Guo, *J. Mater. Sci.* **2023**, *58*, 12271.
[36] X. Zhang, X. Lan, Y. Feng, X. Wang, S. Kong, Z. Xu, Z. Ma, W. Gong, Y. Yao, Q. Li, *Adv. Mater. Interfaces* **2023**, *10*, 2202035.
[37] J. Park, K. J. Kim, *J. Sol-Gel Sci. Technol.* **2024**, *110*, 654.
[38] M. C. Soult, V. Siller, X. Zhu, R. Gehlhaar, P. J. Wojcik, A. Morata, A. Tarancon, P. M. Vereecken, A. Hubin, *J. Electrochem. Soc.* **2022**, *169*, 040501.
[39] P. S. Whitfield, S. Niketic, I. J. Davidson, *J. Power Sources* **2005**, *146*, 617.
[40] B. Song, H. Liu, Z. Liu, P. Xiao, M. O. Lai, L. Lu, *Sci. Rep.* **2013**, *3*, 3094.
[41] X. Zhang, X. Xie, R. Yu, J. Zhou, Y. Huang, S. Cao, Y. Wang, K. Tang, C. Wu, X. Wang, *ACS Appl. Energy Mater.* **2019**, *2*, 3532.
[42] T. Erichsen, B. Pfeiffer, V. Roddatis, C. A. Volkert, *ACS Appl. Energy Mater.* **2020**, *3*, 5405.
[43] Z. Peng, G. Wang, Y. Cao, Z. Zhang, K. Du, G. Hu, *J. Solid State Electrochem.* **2016**, *20*, 2865.
[44] M.-S. Wang, J. Wang, J. Zhang, L.-Z. Fan, *Ionics* **2015**, *21*, 27.
[45] W. Zhang, Z. Zhao, Y. Lei, J. Xing, X. Cao, *Int. J. Electrochem. Sci.* **2020**, *15*, 6188.
[46] Z. Li, K.-S. Oh, J.-M. Seo, W. Qin, S. Lee, L. Zhai, C. Li, J.-B. Baek, S.-Y. Lee, *Nano-Micro Lett.* **2024**, *16*, 265.
[47] S. Zhang, Z. Yin, L. Wang, M. Shu, X. Liang, S. Liang, L. Hu, C. Deng, K. Hu, X. Zhu, *Energy Mater.* **2024**, *4*, 400065.
[48] J. Xu, S. Zhu, Z. Xu, H. Zhu, *Comput. Mater. Sci.* **2023**, *229*, 112426.
[49] Y. Yu, S. Wang, J. Guo, C. Su, X. Liu, W. Bai, H. Bai, R. Wang, *Int. J. Electrochem. Sci.* **2018**, *13*, 9950.
[50] Y. Pan, Y. Li, L. Hu, Y. Yang, J. Guo, S. Yang, *J. Power Sources* **2025**, *650*, 237527.
[51] T. Yi, E. Zhao, Y. He, T. Liang, H. Wang, *Escience* **2024**, *4*, 100182.
[52] S. Wang, H. Hu, P. Yu, H. Yang, X. Cai, X. Wang, *J. Appl. Electrochem.* **2018**, *48*, 1221.
[53] F. Zhang, T. Geng, F. Peng, D. Zhao, N. Zhang, H. Zhang, S. Li, *ChemElectroChem* **2019**, *6*, 731.
[54] Y. Yu, J. Guo, M. Xiang, C. Su, X. Liu, H. Bai, W. Bai, K. Duan, *Sci. Rep.* **2019**, *9*, 16864.
[55] C. Tomon, S. Sarawutanukul, N. Phattharasupakun, S. Duangdangchote, P. Chomkhuntod, N. Joraleechanchai, P. Bunyanidhi, M. Sawangphruk, *Commun. Chem.* **2022**, *5*, 54.
[56] C. Zhan, T. Wu, J. Lu, K. Amine, *Energy Environ. Sci.* **2018**, *11*, 243.
[57] J. Vetter, P. Novák, M. R. Wagner, C. Veit, K. C. Möller, J. O. Besenhard, M. Winter, M. Wohlfahrt-Mehrens, C. Vogler, A. Hammouche, *J. Power Sources* **2005**, *147*, 269.
[58] A. Bhandari, J. Bhattacharya, *J. Electrochem. Soc.* **2017**, *164*, A106.
[59] C. Zhan, J. Lu, A. Jeremy Kropf, T. Wu, A. N. Jansen, Y.-K. Sun, X. Qiu, K. Amine, *Nat. Commun.* **2013**, *4*, 2437.
[60] J. Wang, M. M. Islam, S. W. Donne, *Electrochim. Acta* **2021**, *386*, 138366.